Flow, Turbulence and Combustion manuscript No.
(will be inserted by the editor)

A mesh adaptation strategy to predict pressure losses in LES of swirled flows

Guillaume Daviller · Maxence Brebion · Pradip Xavier · Gabriel Staffelbach · Jens-Dominik Müller · Thierry Poinsot

Received: date / Accepted: date

Abstract Large-Eddy Simulation (LES) has become a potent tool to investigate instabilities in swirl flows even for complex, industrial geometries. However, the accurate prediction of pressure losses on these complex flows remains difficult. The paper identifies localised near-wall resolution issues as an important factor to improve accuracy and proposes a solution with an adaptive mesh h-refinement strategy relying on the tetrahedral fully automatic MMG3D library of Dapogny et *al.* (J. Comput. Phys. 262, 358-378, 2014) using a novel sensor based on the mean dissipation of kinetic energy Φ. Using a joint experimental and numerical LES study, the methodology is first validated on a simple diaphragm flow before to be applied on a swirler with two counter-rotating passages. The results demonstrate that the new sensor and adaptation approach can effectively produce the desired local mesh refinement to match the target losses, measured experimentally. Results shows that the accuracy of pressure losses prediction is mainly controlled by the mesh quality and density in the swirler passages. The refinement also improves the computed velocity and turbulence profiles at the swirler outlet, compared to PIV results. The significant improvement of results confirms that the sensor is able to identify the relevant physics of turbulent flows that is essential for the overall accuracy of LES. Finally, in the appendix, an additional comparison of the sensor fields on tetrahedral and hexahedral meshes demonstrates that the methodology is broadly applicable to all mesh types.

Keywords LES · swirl injector · pressure losses · adaptive mesh refinement

G. Daviller & G. Staffelbach
CERFACS, 42 Avenue Gaspard Coriolis, 31057 Toulouse Cedex 01, France
E-mail: guillaume.daviller@cerfacs.fr

M. Brebion, P. Xavier & T. Poinsot
IMFT, Allée du Professeur Camille Soula, 31400 Toulouse, France

J.-D. Müller
School of Engineering and Materials Science, Queen Mary University of London, E1 4NS, UK

1 Introduction

The design of swirl injectors used in combustion chambers is often based on multiple passages and relies on complex geometrical shapes. The swirler controls a large part of the chamber performances: flame stabilisation, mixing between fuel and air, flame stability, ignition capabilities, etc [1] and its optimisation is a crucial part of an engine design. Large-Eddy Simulation (LES) has become a reference method for the simulation of swirling flows in the last ten years [2–4]. Nevertheless, the prediction of pressure losses in swirl burners using LES remains a challenge for most industrial solvers: errors on pressure losses in swirled systems computed with LES can be surprisingly high as discussed below.

LES have been applied with tremendous success to swirled injectors used in combustion chambers for both non-reacting [5,6] and reacting flows [4,7–9]. Velocity profiles at various positions downstream of the swirled injectors usually match experimental velocity profiles very well, with and without reaction. What is seldom studied, however, is the capability of the LES solvers to predict pressure losses through these systems. These losses are a first order parameter in the design of swirled injectors: excessive pressure losses directly impact the engine efficiency so that predicting them accurately is as important as predicting velocity profiles. Unfortunately, recent studies show that while most LES capture velocity profiles accurately downstream of the swirler, they fail to predict pressure losses through the swirler itself with precision, usually overestimating them by 20 to 50 %. Pressure losses in a swirling system are mainly induced by sudden expansion within the swirler passages, where strong flow directional perturbations occur [10]. Of course, increasing the total number of points inside the swirler helps to improve the accuracy of the prediction of pressure losses, but refining uniformly in the swirler is not affordable. Only few studies have addressed prediction of losses in combustors with complex geometry [10,11], whereas the sensitivity of LE,S to mesh quality is a well-known issue for non-reacting flows [12] as well as for reacting flows [3,13].

Three different approaches are commonly used in Adaptive Mesh Refinement (AMR) strategies in CFD: r-refinement methods where cells of a given mesh are redistributed, p-refinement methods where the order of discretisation is locally increased and h-refinement approaches where cells are subdivided isotropically or anisotropically [14]. In this latter case, a new mesh with a modified density distribution is generated [15,16]. Whereas r- and p-refinement are most useful for dynamic mesh refinement as they do not change the mesh topology, h-refinement and remeshing are very appropriate for static mesh adaptation as they allow to add cells. While h-refinement is the most costly approach, it is the only one which can produce a high-quality mesh that is independent of the initial mesh. AMR methods have been developed for Reynolds Average Navier-Stokes (RANS) methods for a long time [17,18] but they remain a challenge in LES: being able to generate LES meshes on the basis of well-established metrics instead of relying on the intuition of the LES user is probably the overarching question for future LES.

The objective of the present study focuses on this problem for one specific case: non-reacting flows in swirlers. Uniform mesh refinement is not an affordable option, so that adaptive mesh refinement appears as an appropriate tool. In turn, a local mesh refinement approach based on h-refinement requires a sensor which robustly flags all areas relevant to pressure loss inside the swirler, but does not use valuable mesh resources in irrelevant areas. The present work proposes

an adaptive h-refinement method to increase the accuracy of the prediction of pressure losses while keeping the total number of mesh points to a minimum.

The approach employs remeshing which is driven by a sensor based on mean flow data. The sensor considers as Quantity of Interest (QOI) the dissipation of kinetic energy. This QOI is averaged during the simulation and provided as field function to the MMG3D library [19] which carries out the remeshing operations. A new solution is then computed on the refined mesh, and the process is repeated once or twice during a full simulation. This is sufficient to reach an accuracy of a few percent on pressure losses while preserving or improving the quality of all velocity profiles and retaining an appropriate number of cells.

This paper is organised as follows: Section 2 shows why the kinetic energy dissipation is the right mesh metric to predict pressure losses and presents the mesh adaptation procedure where the LES solver is coupled to the tetrahedral mesh refinement code MMG3D. The remeshing methodology is then validated on the canonical case of a simple orifice-plate in Section 3. Section 4 presents first the experimental configuration and the flow parameters for the industrial swirl fuel injector. LES and PIV results are then compared and analyzed. Additionally, as the choice between hexahedral and tetrahedral meshes in LES and CFD is a general CFD topic, a LES on an unstructured fully hexahedral grid for the same industrial burner is shown in the Appendix, highlighting the universality of the adaptation criteria in this paper.

2 Mesh metric for the prediction of pressure losses

As underlined by Mitran [20], the criterion governing grid refinement in CFD should represent the physics of the problem. Due to the unsteady chaotic nature of turbulence, knowing where to refine the mesh in an LES is a complicated question which may depend on the objectives of the simulation: the best mesh to predict far field noise sources is probably not the best mesh to capture pressure losses. Metrics for CFD have been proposed for RANS meshes for a long time [15, 21] and are still studied today [22, 23]. Metrics for LES or DNS have also been derived recently. This can be done either as a dynamic approach, i.e. performed at run time, so that the mesh is adapted to the instantaneous solution (see [24–26]), but can also be done statically, i.e. performed using mean flow characteristics once or twice during the whole simulation [11], as proposed here.

The first step to build a proper QOI adapted to the accurate prediction of pressure losses in swirlers is to identify which physical mechanisms generate these losses. This can be obtained by considering conservation equations for kinetic energy $E_c = (1/2)\rho u_i u_i$ and for entropy s. The instantaneous equation for kinetic energy E_c can be written in incompressible flows as:

$$\underbrace{\frac{\partial E_c}{\partial t}}_{1} + \underbrace{\frac{\partial}{\partial x_j}\left(u_j\left(E_c + P\right)\right)}_{2} = \underbrace{\frac{\partial\left(\tau_{ij}u_i\right)}{\partial x_j}}_{3} + \underbrace{\tau_{ij}\frac{\partial u_i}{\partial x_j}}_{4} \tag{1}$$

where terms (1), (2), (3) and (4) correspond respectively to the temporal variation of the kinetic energy, the mechanical energy flux, the viscous diffusion and the viscous dissipation. The instantaneous entropy equation expressed with the same notations is:

$$\frac{\partial \rho s}{\partial t} + \frac{\partial \rho u_j s}{\partial x_j} = \frac{1}{T}\left(\tau_{ij}\frac{\partial u_i}{\partial x_j} + \frac{\partial}{\partial x_j}\left(\lambda \frac{\partial T}{\partial x_j}\right)\right) \tag{2}$$

Equations 1 and 2 reveal the importance of the viscous dissipation Φ:

$$\Phi = \tau_{ij}\frac{\partial u_i}{\partial x_j} = \frac{\mu}{2}\left(\frac{\partial u_i}{\partial x_j} + \frac{\partial u_j}{\partial x_i}\right)^2 \tag{3}$$

This term is present in the entropy equation and measures the losses due to fluid friction irreversibilities [27–29]. Of course, this is not a surprising result and the dissipation Φ plays a major role in all turbulence theories where it controls the dissipation to the small scales. The aerodynamic community [27,29–32] and the applied mathematicians [33,34], have also been using entropy as a quality indicator for a long time. The dissipation Φ also appears in the kinetic energy equation and rewriting this equation to introduce the total pressure $P_t = P + E_c$ shows that the dissipation Φ is the quantity which controls the dissipation of total pressure and therefore pressure losses:

$$\frac{\partial E_c}{\partial t} + \frac{\partial}{\partial x_j}\left(u_j P_t\right) = \frac{\partial\left(\tau_{ij}u_i\right)}{\partial x_j} + \Phi \tag{4}$$

For a steady flow, the integration of Eq. 4 over the whole computational domain of volume Δ bounded by a surface Σ, with the Ostrogradsky's theorem gives:

$$\int_\Sigma P_t u_i n_i d\sigma = \int_\Delta \frac{\partial\left(\tau_{ij}u_i\right)}{\partial x_j} dV + \int_\Delta \Phi dV \tag{5}$$

Finally, for a case with non-moving walls, the first right-hand side term of Eq. 6, which corresponds to the power of external viscous forces, cancels. The pressure losses are then directly expressed by the integral of the volumetric dissipation rate:

$$Q_v \Delta P_t = \int_\Delta \Phi dV \tag{6}$$

where Q_V is the volume flow rate and ΔP_t is the pressure loss between inlet and outlet sections. Eq. 6 confirms that errors on pressure losses ΔP_t in a simulation are due to the fact that the total dissipation $\int_\Delta \Phi dV$ is not computed with sufficient accuracy. The fact that the dissipation field Φ controls the irreversible losses in the entropy equation as well as the pressure losses in the kinetic energy equations suggests that a proper QOI to use in a metric aiming at adapting meshes to improve pressure losses prediction is the field of Φ: this is the QOI chosen in this paper.

An additional complexity introduced by LES is that the equations used in LES are not Eq. 1. Some differences must be accounted for to construct the QOI to use in an LES:

– Many LES use compressible formulations where additional phenomena (dilatation dissipation for example [35]) contribute to losses. To first order however, it is reasonable to accept, especially for low speed flows, that Φ is the simplest quantity to use for mesh adaptation even if the flow is compressible.

- In the present mesh adaptation strategy, Eq. 1 will be averaged over time to produce a steady field. Therefore the proper QOI is not the instantaneous field Φ but its time averaged field $\overline{\Phi}$.
- Finally, LES does not resolve all spatial scales: the LES field corresponds to a filtered velocity $\tilde{u}_i$ and not the local velocity u_i [36,37]. The filtering operation introduced by LES leads to an expression for dissipation which contains two parts: the first one is produced by the fluctuations resolved on the LES grid and can be written $\phi = \mu \left(\frac{\partial \tilde{u}_i}{\partial x_j} + \frac{\partial \tilde{u}_j}{\partial x_i} \right)^2$. The second contribution to dissipation corresponds to the unresolved part and can be written $\varphi = \mu_t \left(\frac{\partial \tilde{u}_i}{\partial x_j} + \frac{\partial \tilde{u}_j}{\partial x_i} \right)^2$ where μ_t is the local turbulent viscosity. Therefore a proper expression for the QOI is the time averaged of the sum of these two contributions: $\overline{\tilde{\Phi}} = \overline{\phi + \varphi}$:

$$\overline{\tilde{\Phi}} = \overline{(\mu + \mu_t) \left(\frac{\partial \tilde{u}_i}{\partial x_j} + \frac{\partial \tilde{u}_j}{\partial x_i} \right)^2} \tag{7}$$

  This is the QOI used in the following sections. It is expected to provide a metric leading to mesh refinement in zones where $\overline{\tilde{\Phi}}$ will be large so that the precision of pressure losses, which are controlled by this field, will improve. Interestingly, results show that the prediction of the velocity fields is also more accurate and suggest that this metric improves the quality of all results and not just of pressure losses.

In practice, the implementation of the metric in the LES code AVBP is performed as follows (Fig. 1). From the time-averaged dissipation field $\overline{\tilde{\Phi}}$, a dimensionless variable $\Phi^\star$ is first defined as:

$$\Phi^\star = \left[1 - \left(\frac{\overline{\tilde{\Phi}} - \overline{\tilde{\Phi}}_{\min}}{\overline{\tilde{\Phi}}_{\max} - \overline{\tilde{\Phi}}_{\min}} \right) \right]^\alpha, \quad \Phi^\star \in [0:1] \tag{8}$$

where the parameter α in Eq. 8 scales the value of $\Phi^\star$ in order to ensure continuous variation of QOI and to obtain smoother stretching of the cells size in the new mesh. The values $\overline{\tilde{\Phi}}_{\min}$ and $\overline{\tilde{\Phi}}_{\max}$ correspond to the minimum and maximum of the time-averaged dissipation field $\overline{\tilde{\Phi}}$ measured in the whole computational domain, respectively. Then the maximum factor to divide the volume of the tetrahedral cells is imposed by the variable ϵ in the metric:

$$\text{metric} = \Phi^\star (1 - \epsilon) + \epsilon \tag{9}$$

Typical range of values used for these two terms in this study are $0.3 \leq \epsilon \leq 0.7$ and $30 \leq \alpha \leq 100$. The value of ϵ fixes the maximum refinement: no cell with a volume Δ is allowed to be reduced to less than $\epsilon\Delta$. The value of α controls the dilatation of the cells allowed on the mesh. The MMG3D library [19] then interpolates the mesh size to use from the prescribed metric on the current mesh. Finally, the MMG3D library is used to generate an entirely new mesh. The mesh refinement strategy is shown on Fig. 1. No restriction on the number of tetrahedra is specified but a minimal cell volume is fixed. This parameter is simply defined using the maximum of the metric and the minimal cell volume of the mesh before adaptation. The AVBP code uses a compressible formulation with explicit time-stepping and is hence subject to a CFL condition based on the fastest acoustic wave. To maintain an appropriate time-step Δt, the local

mesh size must not be too small. Only isotropic subdivisions of the tetrahedra are considered to preserve the mesh quality [38]. While anisotropic remeshing can be very appropriate in producing high-aspect ratio cells aligned with strong gradients in steady flow [16], the present computations are unsteady and the extreme element angles found in anisotropic tetrahedral meshes would adversely affect accuracy. All simulations in sections 3 and 4 are performed using the compressible cell-vertex Navier-Stokes solver AVBP [39,40]. The third-order scheme TTGC [41] is used on a fully tetrahedral mesh. In order to remove spurious numerical oscillations, an artificial viscosity operator of 2nd and 4th order is also applied according to a local sensor [41]. At the inlet and outlet boundaries, the classical Local One-Dimensional Inviscid (LODI) Navier-Stokes Characteristic Boundary Conditions (NSCBC) are used [42]. These boundaries conditions are derived from the time-dependent boundary conditions proposed by Thompson [43] and are non-reflective, based on the work of Rudy & Strikwerda [44]. An eddy-viscosity approach is considered for the SubGrid-Scale (SGS) stress, based on the SIGMA model [45]. The choice of SIGMA is motivated by its low computational cost and its good results compared to the Dynamic Smagorinsky model and experiments [46–48]. The SIGMA model is computed from the singular values of the local velocity gradient tensor. No-slip adiabatic conditions are applied at all walls.

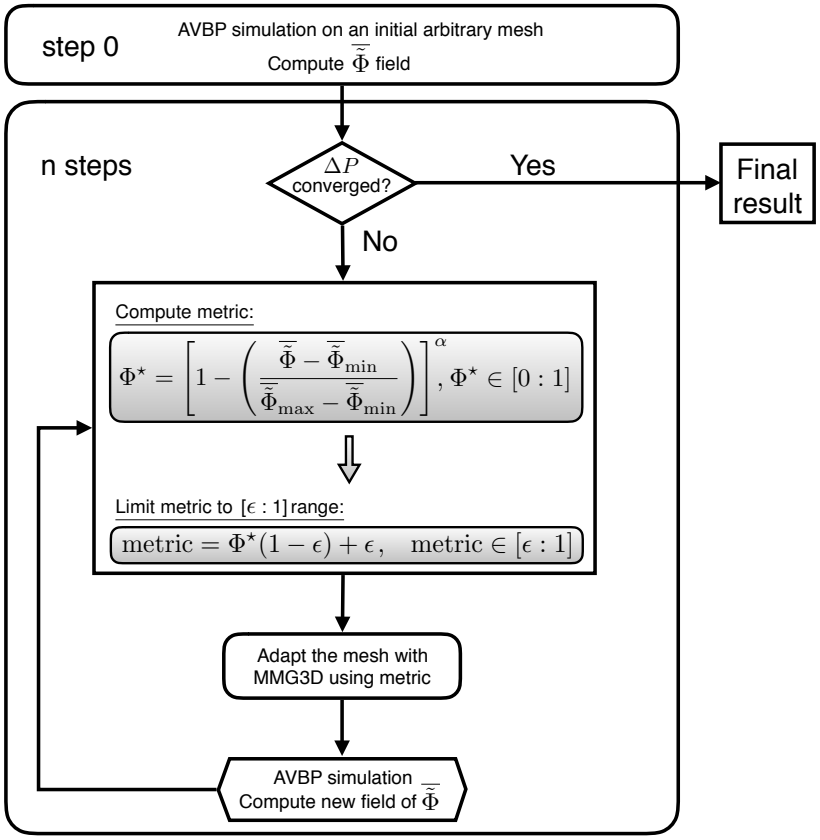

Fig. 1 Mesh adaptation procedure.

3 Validation on a canonical test case: pressure losses through a diaphragm

The AVBP-MMG3D strategy is first validated for the canonical test case of an orifice plate in a straight duct (Fig. 2). The evaluation of the pressure losses through a diaphragm is a usual task in the industry to measure flow rates. Due to the simplicity of the geometry, many pressure loss correlations derived from experiment are available in the literature [49,50]. In order to compare LES and experimental data, a series of experimental measurement were performed on a diaphragm to make sure that pressure losses were evaluated correctly.

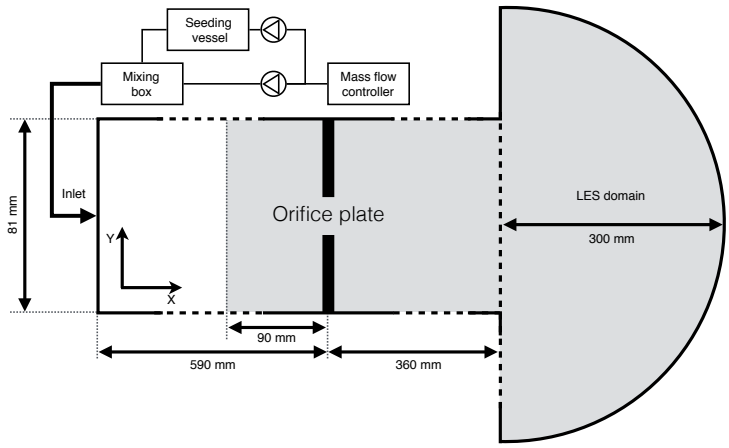

Fig. 2 Schematic view of the experimental setup of the diaphragm. The shaded area correspond to the LES domain.

The geometry of the sharp-edged orifice is defined by a single circular hole of diameter $d = 18\,\text{mm}$ and thickness $t = 2\,\text{m}$, centered in a pipe with an inner diameter of $D = 81\,\text{mm}$. The air stream is controlled with a Brooks mass flow controller for a range of mass flow rates $0.43\,\text{g}\cdot\text{s}^{-1} \leq \dot{m} \leq 3.55\,\text{g}\cdot\text{s}^{-1}$. Flow rates are measured with an uncertainty of 1%. The flow is then guided in a 590 mm long tube upstream of the orifice. The latter expands in a tube having a length of 360 mm which is opened to the atmosphere. Total pressure loss through the orifice is measured with an electronic micro-manometer, and with an uncertainty smaller than 0.25%. The experimental pressure drop curve measured with this device is displayed on Fig. 3. The Idel'Cik correlation [49] for orifice plate and Reynolds number $Re < 10^5$ is in agreement with the LES results.

The mesh refinement procedure is tested first for a mass flow rate of $\dot{m} = 3.55\,\text{g}\cdot\text{s}^{-1}$ where the pipe flow upstream of the orifice-plate is characterised by a bulk velocity $U_b = 0.55\,\text{m}\cdot\text{s}^{-1}$ and a Reynolds number $Re_D = U_b D/\nu = 3000$. The ambient pressure and temperature of the experiment are $P = 101150\,\text{Pa}$ and $T = 292\,\text{K}$. The computational domain is shown on Fig. 2. The inlet plenum is truncated at $x = -90\,\text{mm}$ in the LES. A semi-hemisphere, defined by a radius of ($r = 0.3\,\text{m}$) is added at the duct outlet in order to mimic the atmosphere in the experiment and dissipate free-jet flow fluctuations. Downstream of the orifice-plate, centered at $x = 0\,\text{mm}$ (the upstream inlet edge is at $x = -1\,\text{mm}$), a

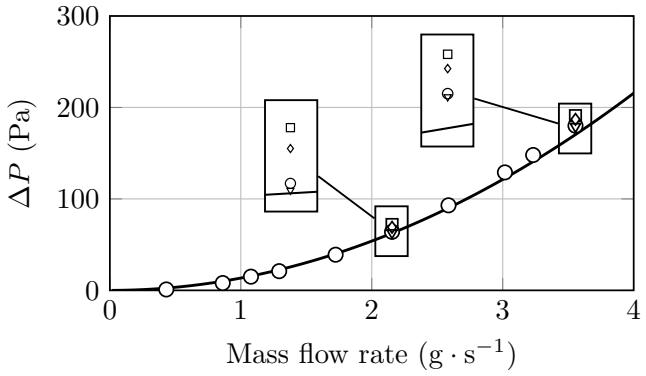

Fig. 3 Experimental pressure loss evolution across the orifice plate for different mass flow rates. Comparison of the measured values (○) with the Idel'Cik model [49] (——) and the LES results for the coarse (□), the adapted 1 (◊) and the adapted 2 (▽) meshes.

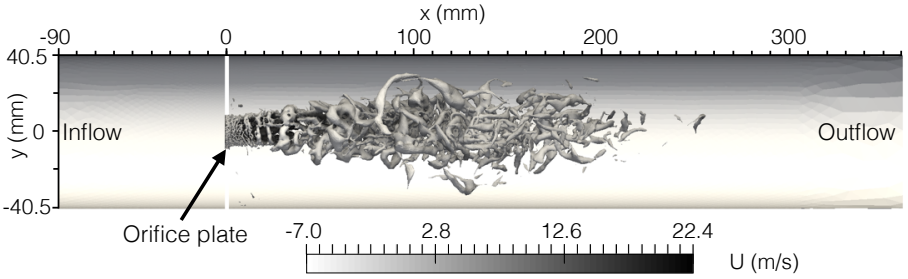

Fig. 4 LES of the orifice-plate at $\dot{m} = 3.55\,\mathrm{g} \cdot \mathrm{s}^{-1}$. The instantaneous flow is represent using Q-criterion $Q = 1.62(U_j/D_j)^2$ colored by axial velocity, on mesh AD 2.

jet-plume flow develops as expected. This is shown using Q-criterion (as defined by Hunt *et al.* [51]) on Fig. 4.

In this test case, the target pressure loss is obtained in two adaptation steps and three LES. Table 1 summarises the parameters and the cost. From an initial coarse mesh (Fig. 5), a first adapted mesh "AD 1" is obtained. The central picture in Fig. 5 shows that the mesh refinement follows the distribution of viscous dissipation $\overline{\tilde{\Phi}}$ obtained on the coarse mesh. This first refinement step leads to an overestimation of the pressure drop compared to the experiment of only 3.8% while it was 6.1% on the coarse mesh. Finally, an acceptable discretisation is obtained in the second step and the mesh "AD 2". The error on the predicted losses is less than 1%. Figure 6 shows radial profiles of the mean and r.m.s. axial velocity across the orifice at the leading edge ($x = -1\,\mathrm{mm}$), the center ($x = 0\,\mathrm{mm}$) and the trailing edge ($x = 1\,\mathrm{mm}$), respectively. Only the last mesh "AD 2", allows the apparition of the "vena-contracta" effect, with a flow separation zone across the diaphragm. Indeed, no reverse flow appears downstream the leading edge of the diaphragm at $x = 0\,\mathrm{mm}$ and $x = 1\,\mathrm{mm}$ with the coarse and AD 1 mesh.

Moreover, a remarkable change is observed for the mean kinetic energy dissipation field between mesh AD 1 and AD 2 on Fig. 5. The solution on mesh AD 1 would suggest that a persistent shear layer has been captured well at the orifice

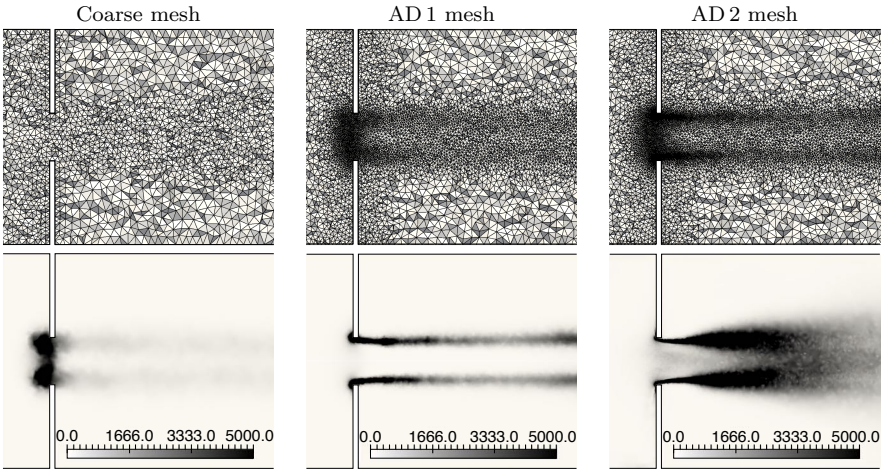

Fig. 5 Orifice-plate test case at $\dot{m} = 3.55\,\mathrm{g}\cdot\mathrm{s}^{-1}$: zoom on the mesh on the orifice for each LES (top images) and mean kinetic energy dissipation $\overline{\tilde{\Phi}}$ (bottom images) in $\mathrm{W}\cdot\mathrm{m}^{-3}$.

and is then swept downstream. AD 2 refinement leads to a mesh which is refined much more close, to the orifice plate: this allows the growth of Kelvin-Helmholtz instabilities and a rapid transition to a fully developed turbulent jet-plume. This is in agreement with the spectral power density obtained from the axial velocity signal recorded at $x = 2d$ and $r = 0.5d$ for the three meshes (Fig. 7). Only the axial velocity spectrum of mesh AD 2 is fully broadband and exhibit a typical $k = -5/3$ slope over one decade. Mesh AD 1 allows the development of instabilities, characterised by a narrow band with a maximum for $f = 700\,\mathrm{Hz}$, but no inertial zone is found in the spectrum. The result for the coarse mesh suggests that the flow remains fully laminar.

Table 1 Summary of the mesh adaptation LES on the orifice-plate at $\dot{m} = 3.55\,\mathrm{g}\cdot\mathrm{s}^{-1}$.

	Coarse	AD 1	AD 2
α	—	100	50
ϵ	—	0.3	0.4
$\mathrm{T_{init}}$ (s)	1.5	0.3	0.3
$\mathrm{T_{stat}}$ (s)	0.5	0.5	0.5
time step ($\times 10^{-6}$ s)	1.4	0.41	0.13
number of cells ($\times 10^{6}$)	0.71	1.55	2.75
number of CPU hours	3h06	5h30	19h
number of cores	256	720	1152
ΔP error	6.1%	3.8%	−0.5%

The adaptation approach was repeated at a mass flow rate of $\dot{m} = 2.15\,\mathrm{g}\cdot\mathrm{s}^{-1}$ to further check its validity (cf. Fig. 3). The experimental target is also reached in two mesh refinement steps with a final error of 1.6%.

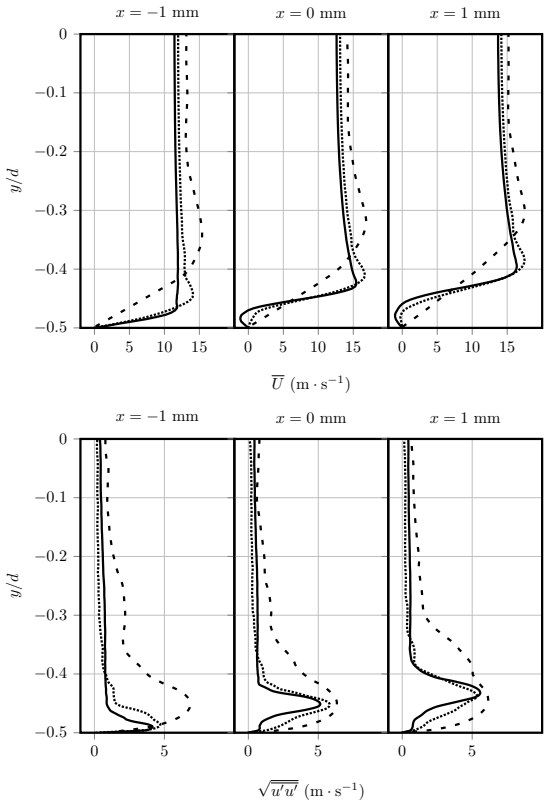

Fig. 6 Orifice-plate test case at $\dot{m} = 3.55\,\mathrm{g}\cdot\mathrm{s}^{-1}$: Up, radial distribution of axial mean velocity across the orifice. Down, radial distribution of r.m.s. axial velocity. Coarse mesh (- - - -); mesh AD 1 (·····) and mesh AD 2 (——).

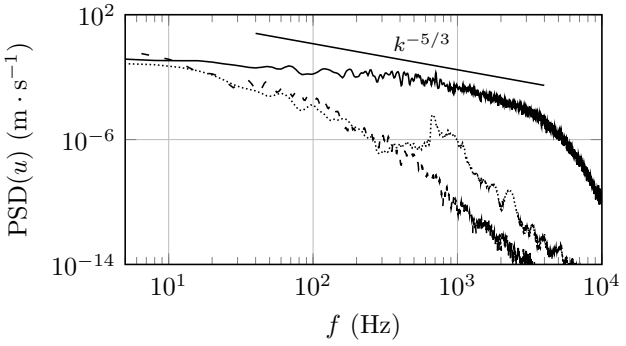

Fig. 7 Orifice-plate test case at $\dot{m} = 3.55\,\mathrm{g}\cdot\mathrm{s}^{-1}$: power spectral density of the axial velocity in the jet-plume shear layer at $x = 2d$ and $r = 0.5d$. Coarse mesh (- - - -); mesh AD 1 (·····) and mesh AD 2 (——).

4 Pressure losses in a swirled injector

4.1 Description of the swirler

A schematic view of the radial swirl injector used for this study is shown in Fig. 8. The air entering the swirler is divided into two passages: the primary flow

passes through the inner region of the passages with eight tangential vanes. The secondary flow passes through the outer passages with the same number of vanes but with counter-rotating swirl direction. No fuel is injected for these tests: in order to replace the fuel injection system, a plug is inserted in the primary flow along the centerline of the swirler producing a recess of 14 mm with respect to the exit plane.

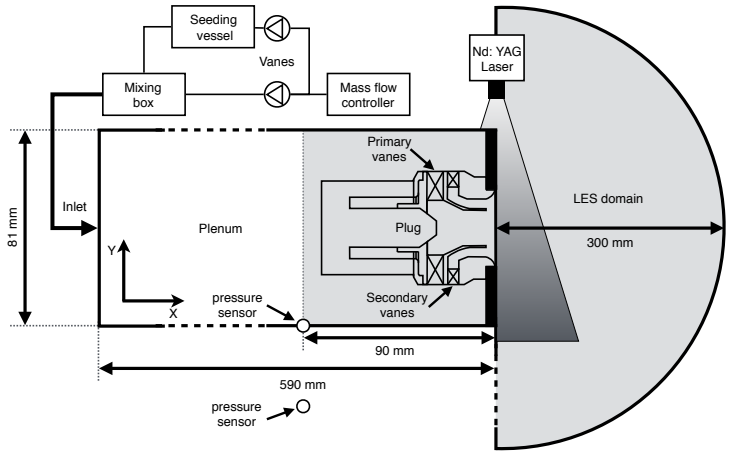

Fig. 8 Schematic view of the experimental setup, swirler device and LES domain. The longitudinal (xOy) PIV plane is highlighted. The shaded area corresponds to the LES domain.

4.2 Experimental set-up

The flow is guided in a 590 mm plenum (Fig. 8) before reaching the swirl injection system with an exit diameter of $D = 0.018$ m which blows into the atmosphere. PIV measurements of the velocity field have been performed downstream of the injector, along a longitudinal (xOr) plane (Fig. 8). A double cavity Nd:YAG laser (Quantel Big Sky) operating at 532 nm fires two laser beams, with a delay varying between 4 μs and 11 μs according to the operating conditions. The beam is expanded through a set of fused silica lenses (spherical and diverging). Because of the important out-of-plane velocity component, the laser sheet was intentionally thickened to approximately 1 mm. Olive oil particles (typical size of $1 - 2\,\mu$m) were seeded through the various flow injections systems (by means of venturi seeders). Mie scattering is collected on a 4 Hz PCO-Sensicam, operating with a resolution of 1280×600 pixels for the longitudinal plane. A f/16 182 mm telecentric lens (TC4M64, Opto-engineering) is used to reduce parallax displacements occurring with classical lenses. PIV images are processed with a cross-correlation multi-pass algorithm (Davis 8.2.3), resulting in a final window of $16 \times 16\,\text{px}^2$ and a 50% overlap. 1320 images are collected over a region of $20 \times 32\,\text{mm}^2$ with a vector resolution of 0.4 mm. The pressure loss through the swirler is measured with the differential pressure sensor used for the orifice-plate test case (see section 3). The two pressure sensors are located on the wall (flush

mounted) of the plenum and in the atmosphere, respectively, at 90 mm from the swirler exit (Fig. 8).

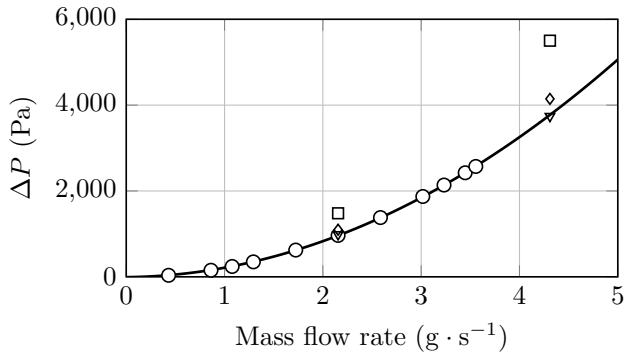

Fig. 9 Pressure loss evolution through the swirler: experimental data (○), fit function (——), LES results for the coarse (□), the adapted 1 (◇) and the adapted 2 (▽) meshes.

4.3 Flow parameters

The pressure losses of the swirled injector system are measured over a range of mass flow rates $0.43\,\mathrm{g \cdot s^{-1}} \leq \dot{m} \leq 3.55\,\mathrm{g \cdot s^{-1}}$. PIV measurements are performed at three mass flow rates $\dot{m} = 2.15,\ 3.22,\ 4.29\,\mathrm{g \cdot s^{-1}}$ with an ambient temperature and pressure of $T = 298\,\mathrm{K}$ and $P = 101150\,\mathrm{Pa}$, respectively. First, LES are performed at $\dot{m} = 4.29\,\mathrm{g \cdot s^{-1}}$. The bulk velocity at the nozzle exit for this case is defined as $U_b = \dot{m}/(\rho A) = 13.9\,\mathrm{m \cdot s^{-1}}$. The theoretical swirl number is $S = 0.76$ (estimated from the definition given by Merkle [52]) and a Reynolds number based on the bulk velocity and the swirler exit diameter is $Re = U_b D/\mu \sim 14 \times 10^3$. The inlet plenum is truncated to $x = -90\,\mathrm{mm}$ in the LES. The experimental mean axial velocity profile at this position is measured using hot-wire anemometry data (Fig. 10). A fit function is then used as inlet boundary condition in the LES. Downstream of the swirler exit, the LES domain is bounded by a semi-hemisphere with a radius $r = 0.3\,\mathrm{m}$.

4.4 Pressure losses

Fig. 11 shows the time evolution of the instantaneous pressure loss measured in the LES, for one reference case where the flow rate is $4.29\,\mathrm{g \cdot s^{-1}}$. The pressure loss evolves during the coarse mesh computation until its average becomes steady with the value overestimated by 46%, compared to the experiment. As observed by many LES users in recent years [11,10], the pressure losses error obtained on a first arbitrary mesh can be very large and the 46% error measured here is not acceptable. The application of the refinement method corrects this problem: pressure losses change abruptly when the mesh is refined for the first time to AD 1 and a second one to AD 2. The error on the pressure losses drops to 10% for AD 1 and finally to less than 1% for AD 2. To investigate mesh convergence,

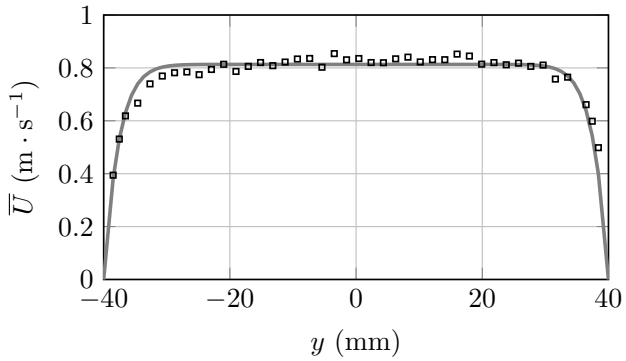

Fig. 10 $\dot{m} = 4.29\,\mathrm{g}\cdot\mathrm{s}^{-1}$ case: mean axial velocity profile inside the plenum at $x = -90\,\mathrm{mm}$ from hot-wire measurement (▫), fit function (——) used as inlet condition in the LES.

an additional adaptation step AD 3 was performed. The pressure losses predicted on this mesh are again in agreement with the experiment (less than 1% of error). These results and the values for the parameters α and ϵ, used to build the mesh refinement metric (cf. Fig. 1) are summarised in table 3.

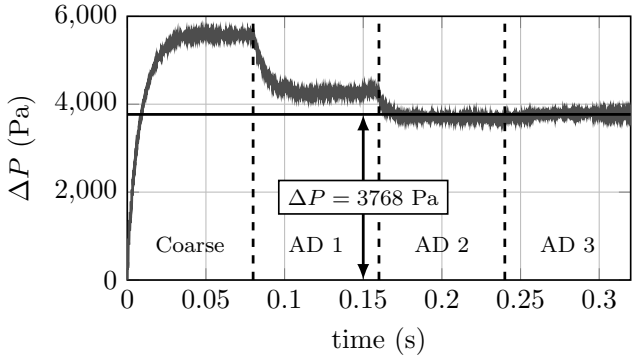

Fig. 11 $\dot{m} = 4.29\,\mathrm{g}\cdot\mathrm{s}^{-1}$ case: Evolution of the pressure loss computed with LES as a function of time and comparison with the target experimental value (straight solid line). The pressure signal is recorded in the upstream plenum at the wall ($x = -50\,\mathrm{mm}$ and $r = 40.5\,\mathrm{mm}$). The mesh is refined by the AVBP-MMG3D three times during the whole procedure.

In addition, in order to assess the numerical uncertainty on the pressure losses prediction, the Grid Convergence Index (GCI) is also computed using the procedure described by Celik et *al.* [53]. The GCI is defined as:

$$\mathrm{GCI} = \frac{1.25 e_a}{r^p - 1} \tag{10}$$

where the approximate relative error e_a between two meshes is defined using pressure losses ΔP as key variable and the grid refinement factor r is defined using the number of cells h of each mesh. The apparent order p is computed using a fixed point algorithm as suggested in [53]. The discretisation uncertainty on

ΔP for mesh AD 1, AD 2 and AD 3 are 7.8%, 1% and 0.05% which corresponds to $\pm 327.2\,\mathrm{Pa}$, $\pm 40.4\,\mathrm{Pa}$ and $\pm 2.1\,\mathrm{Pa}$, respectively.

An important parameter of the LES is the evaluation of the flow characteristic time $\tau_F = D/U_b = 1.3\,\mathrm{ms}$. The simulation time based on this value need to be chosen sufficiently long for the flow to reach steady state as well as the averaged time needed to gather samples in the LES[1]. Fig. 11 shows that the flow adapts to all changes of mesh within 30 τ_F. All statistics used in the rest of the paper were gathered over a period of 40 ms corresponding to 30 flow-through times.

The four meshes (coarse, AD 1, AD 2 and AD 3) are displayed in Fig. 12. As expected, mesh refinement is performed in regions where the total mean dissipation $\overline{\widetilde{\Phi}}$ is large, allowing to resolve the field of $\overline{\widetilde{\Phi}}$ with precision, thereby increasing the precision of the pressure loss evaluation. The convergence of the process can be clearly observed: meshes and results on AD 2 and AD 3 are almost similar.

The automatic refinement procedure AVBP+MMG3D was also applied to an other flow rate at $\dot{m} = 2.15\,\mathrm{g}\cdot\mathrm{s}^{-1}$. Fig. 9 displays the values of the experimental pressure loss vs flow rate compared to the values obtained by the LES for each refinement step. All values of pressure losses correspond to the average pressure loss measured over at least 30 flow-through times (Fig. 11 shows that this time is sufficient for the pressure loss to converge). The procedure appears to be robust for all cases tested here: the refinement procedure leads systematically to small errors compared to the experiment. Note that the procedure is unmodified for all cases: this is a fully automatic method determining a sufficiently resolved mesh in terms of pressure losses, independent of the LES user.

Moreover, in most cases, two refinement steps are sufficient to reach the target so that the simulation costs remain comparable to a normal simulation where the user would try to refine the grid using intuition. Obviously, it is also much cheaper than a brute-force strategy where the whole mesh would be refined homogeneously: here, the homogeneous mesh having the same refinement everywhere as mesh AD 2 has in the swirler region would require 1.4 billion points. The next section shows that the mesh refinement procedure allows also to better predict the velocity field in the chamber itself.

4.5 Velocity fields

The previous section has shown that the AVBP+MMG3D tool was able to produce an acceptable mesh for the pressure loss because it allowed a proper resolution of the time-averaged dissipation field. It is to be expected that with a correct resolution of the mixing phenomena, not only pressure losses but also velocity fields will be predicted more accurately.

[1] In the experiment, all measurements were performed over 110 mm, corresponding to very long times compared to τ_F.

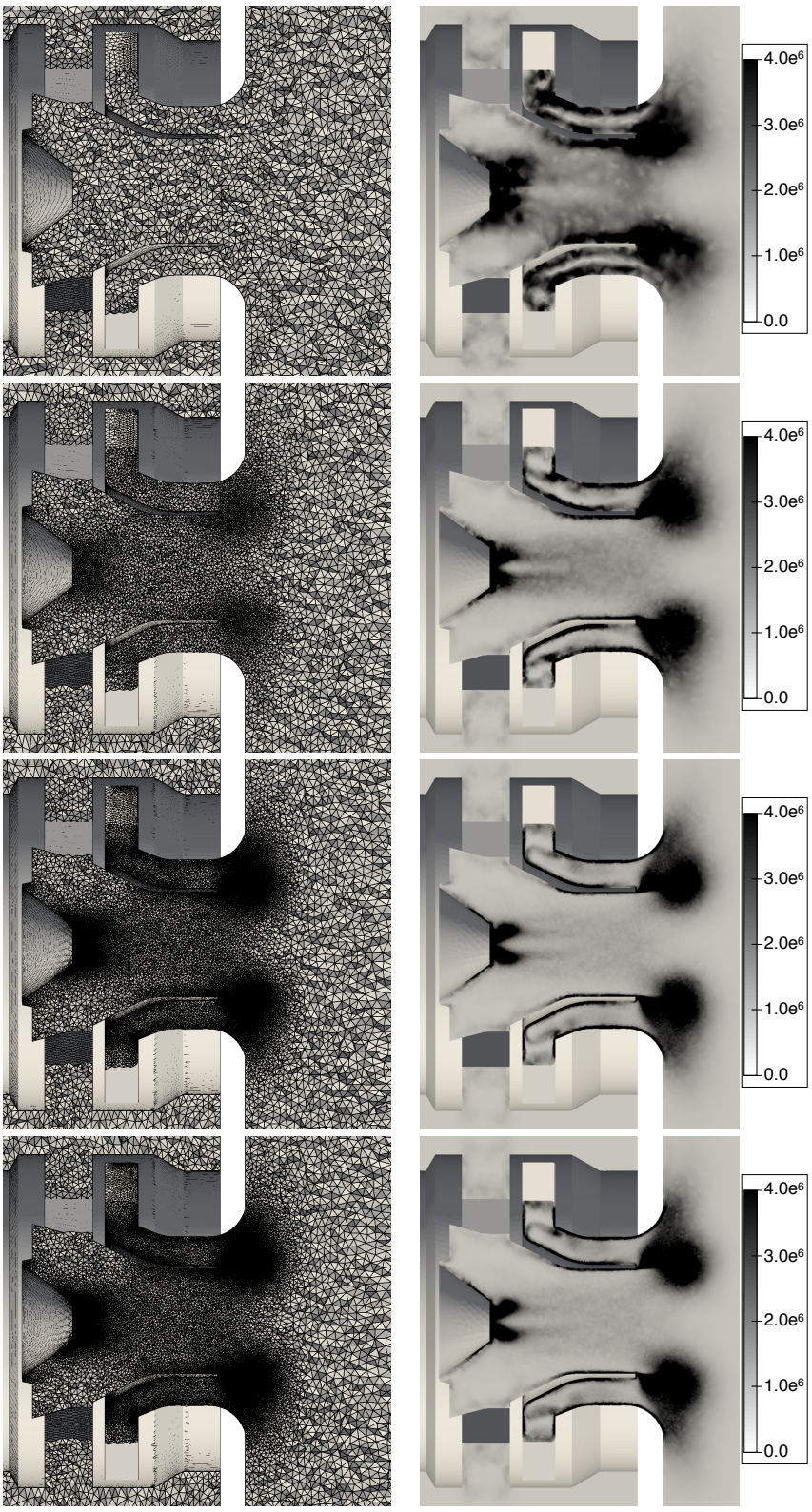

Fig. 12 $\dot{m} = 4.29\,\mathrm{g}\cdot\mathrm{s}^{-1}$ case: meshes (left) and fields of $\overline{\tilde{\Phi}}$ in $\mathrm{W}\cdot\mathrm{m}^{-3}$ (right) for the coarse, AD 1, AD 2 and AD 3 meshes in the central plane of the swirler, from top to bottom, respectively.

To assess this aspect, PIV measurements were performed in the experimental setup (section 4.2) for the $\dot{m} = 4.29\,\mathrm{g}\cdot\mathrm{s}^{-1}$ case and compared to the LES velocity fields on the coarse, AD 1 and AD 2 meshes (AD 3 gave results which are very similar to AD 2). The accuracy of the PIV data was carefully checked by investigating the effects of the measurement windows. Results (table 2) exhibit less than 9% of error on the mass flow rates recover from PIV compared to the target imposed by the mass flow controller at the plenum inlet in the experiement. Fig. 13 compares the mean axial velocity field from PIV and LES (on the AD 2 mesh) in the vicinity of the swirl injector. Results are in excellent agreement. Indeed, in both cases, a strong flow reversal due to vortex breakdown dominates downstream of the exhaust of the primary swirler, which is as expected for flows with a swirl number $S > 0.6$. This very compact reverse flow zone is associated with high turbulence levels [54].

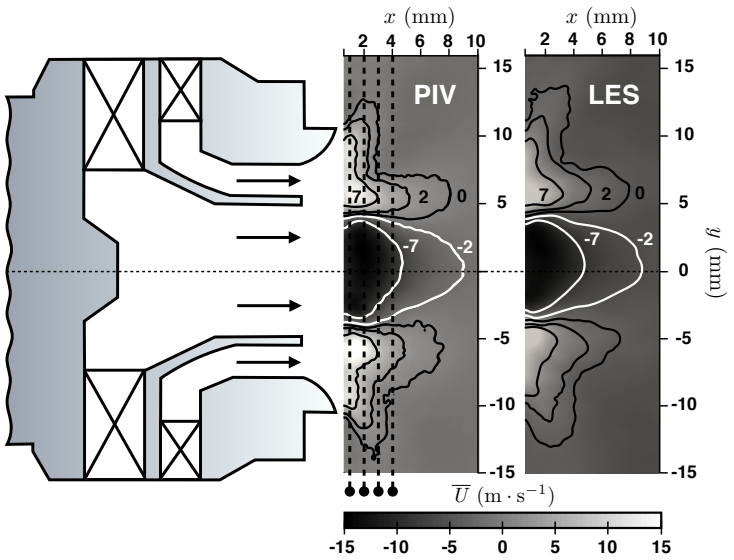

Fig. 13 Comparison of the mean axial velocity from PIV measurement (center) and LES on AD 2 mesh (right) for the $\dot{m} = 4.29\,\mathrm{g}\cdot\mathrm{s}^{-1}$ case. A schematic representation of the swirl injector is depicted on the left. White lines denotes negative mean velocity contours at -7 and $-2\,\mathrm{m}\cdot\mathrm{s}^{-1}$. Positive and zero mean velocity contours of 7, 2 and $0\,\mathrm{m}\cdot\mathrm{s}^{-1}$ are shown with black line. Dashed-lines identify the position of the measurement cross-sections downstream of the exit plane at $x = 1, 2, 3, 4\,\mathrm{mm}$.

Table 2 Error on the experimental mass flow rates recover from PIV result.

Target mass flow rates ($\mathrm{g}\cdot\mathrm{s}^{-1}$)	PIV mass flow rates ($\mathrm{g}\cdot\mathrm{s}^{-1}$)	error (%)
4.29	3.99	7.0
3.22	2.95	8.4
2.15	2.04	5.1

Even if the mean PIV data reveal a smooth averaged field, a visualisation of the instantaneous structures obtained by LES for the same regime (Fig. 14) shows that the flow is highly turbulent with multiple structures developing in the breakdown zone.

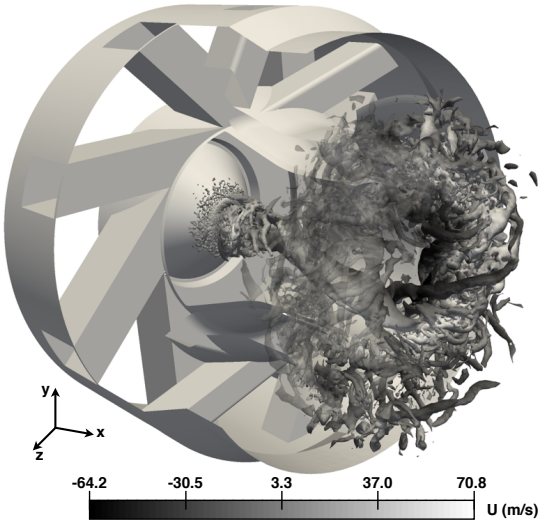

Fig. 14 LES of the swirler on AD 2 mesh: Q-criterion $Q = 1.67 \times 10^4 (U_b/D)^2$ colored by axial velocity for the $\dot{m} = 4.29\,\mathrm{g} \cdot \mathrm{s}^{-1}$ swirler case.

Fig. 15 shows that the precision of the LES, in terms of velocity fields, also increases with mesh refinement levels defined by the AVBP+MMG3D procedure. This is particularly obvious on the mean axial velocity profile at $x = 1\,\mathrm{mm}$ for $-5\,\mathrm{mm} \leq y \leq 5\,\mathrm{mm}$. Nevertheless, the differences between simulation and PIV results in the shear regions may be explained by a limitation of the PIV spatial resolution [55,56]. The LES results for the radial profiles of axial velocity on the AD 2 and AD 3 meshes gives similar fields, again confirming grid convergence for the adaptation for this feature. The swirl number is computed from these mean values at $x = 2\,\mathrm{mm}$ using the method given in [57]. The experimental swirl number is $S_{PIV} = 0.77$, which is very close to the theoretical values $S = 0.76$. The simulated swirl number for the mesh coarse, AD 1, AD 2 and AD 3 are $S_{LES} = 0.62, 0.88, 0.79$ and 0.75, respectively. This means that the swirl motion, which drives the characteristics of this type of flow [58], is correctly reproduced by the LES (see error in table 3) and better predict with this mesh refinement strategy. A similar conclusion can be drawn for the radial profiles of turbulence intensities given in Fig. 16. The predictability of these quantities is clearly improved by refining the mesh (at $x = 3\,\mathrm{mm}$ and $x = 4\,\mathrm{mm}$ for example). More quantitatively, the relative error in the L^2 norm is computed on these profiles at $x = 3\,\mathrm{mm}$. This error is defined by:

$$error_{L^2}(f)\,(\%) = \sqrt{\frac{\int_{y_1}^{y_2} (f_{exp}(y) - f_{LES}(y))^2 dy}{\int_{y_1}^{y_2} (f_{exp}(y))^2 dy}} \tag{11}$$

where $y_1 = 0\,\text{mm}$ and $y_2 = 15\,\text{mm}$ are the lower and upper limits of the integral. Results are resumed in table 3 and show that L^2 norm error is clearly reduced by mesh adaptation. This confirms that capturing the flow features that govern pressure losses through the swirler passages is sufficient for a good prediction of velocity fields further downstream in the chamber. This is not an obvious result: most mechanisms controlling pressure losses occur within the swirler passages where separation on the vanes change the effective sections and directly affect pressure losses. On the other hand, velocity and temperature profiles in the chamber downstream of the swirler are expected to be controlled by the local resolution in the chamber itself and not in the swirler. It is interesting to observe that an improved resolution within the swirler also increases the quality of the velocity profile far downstream of the swirler passages. This suggests that the mesh refinement metric for the pressure losses based on the kinetic energy dissipation provides most if not all of the refinement information needed to predict the flow with accuracy.

Table 3 Summary of the mesh adaptation LES on the swirler

	Coarse	AD 1	AD 2	AD 3
α	—	30	30	30
ϵ	—	0.3	0.3	0.7
T_{init} (s)	0.04	0.04	0.04	0.04
T_{stat} (s)	0.04	0.04	0.04	0.04
time step ($\times 10^{-7}$ s)	1.0	1.0	0.35	0.23
number of cells ($\times 10^6$)	1.4	3.1	10.8	14.7
number of CPU hours	6h22	11h44	20h20	33h40
number of cores	240	240	1140	1728
ΔP error	46%	10%	−0.7%	0.8%
error on swirl number S at $x = 2\,\text{mm}$	18.5%	15.5%	4.3%	1.0%
$error_{L^2}(\sqrt{\overline{u'u'}})$ at $x = 3\,\text{mm}$	11.2%	16.1%	5.8%	5.1%
$error_{L^2}(\sqrt{\overline{v'v'}})$ at $x = 3\,\text{mm}$	11.1%	8.2%	4.6%	4.3%
GCI	—	7.8%	1%	0.05%

4.6 Evaluation of costs

The previous sections have shown that the AVBP+MMG3D procedure provides accurate predictions of pressure losses as well as of velocity and turbulence profiles. A natural question is to determine the cost of this procedure: going from a coarse mesh to refined meshes increases the number of nodes and therefore the overall cost of the simulation. Table 3 summarises the number of cells and the CPU cost (number of hours to compute one flow-through time[2]) on all grids used for the $\dot{m} = 4.29\,\text{g}\cdot\text{s}^{-1}$ case. Obviously the cost per flow through time increases

[2] All CPU costs are given on a single processor. Most runs were performed on 500 to 1000 processors but the parallel efficiency is almost unity for these cases so that the total CPU cost is a good measure of the mesh efficiency.

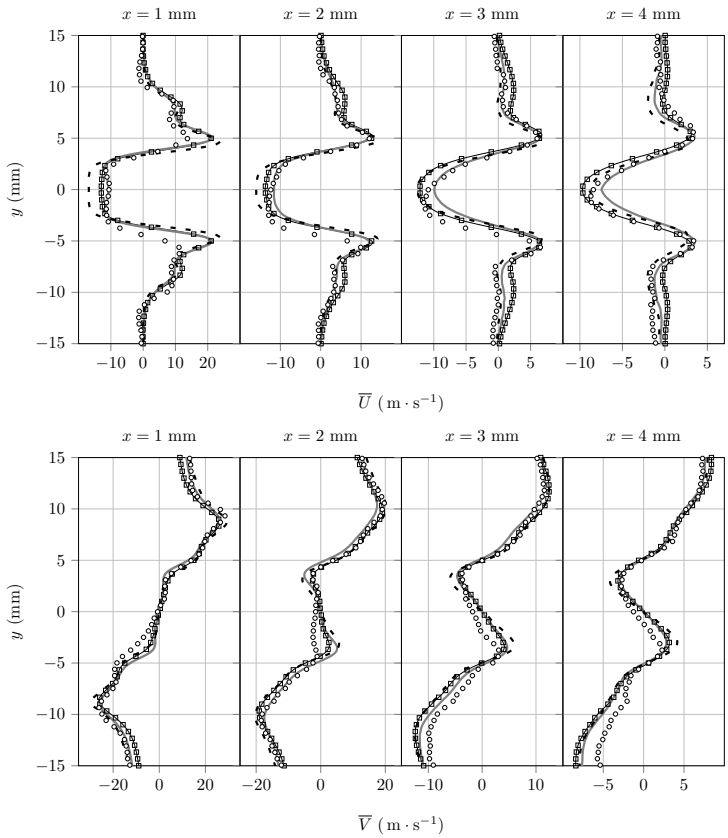

Fig. 15 $\dot{m} = 4.29\,\mathrm{g}\cdot\mathrm{s}^{-1}$ case: comparison of the radial distribution of mean axial (top) and tangential (bottom) velocity at four axial locations (from left to right $x = 1, 2, 3, 4\,\mathrm{mm}$). Coarse mesh (- - -); mesh adapted AD 1 (—□—); mesh adapted AD 2 (——) and experiments PIV (○).

when the mesh is refined. The increase is not proportional to the number of cells as the total time needed on each grid to achieve statistical convergence decreases because the initial flow is interpolated from the converged-average state on the previous mesh and hence is close to its own converged-average state. As a result, the cost of the refined mesh cases remains affordable to improve the capture of physical phenomena relevant to pressure losses.

Another relevant question is whether the proposed AVBP+MMG3D refinement algorithm is more efficient than a purely intuitive mesh refinement method, as typically performed manually by the user based on strong gradients in pressure or velocities. Looking at the various meshes created by the AVBP+MMG3D method (Fig. 12) shows that the method adds points in places which are not obvious to guess: they correspond to regions where $\widetilde{\overline{\Phi}}$ is large and these regions, and their extent, do not correlate with easily identified flow-features. For example, not all shear layers are refined to the same extent, but only those that are highly relevant for pressure losses. As a result, an important aspect of the present refinement procedure is to offer a systematic and robust, user-independent method to optimise meshes for swirler computations. It is acknowledged that while certain

users who have very good knowledge of a particular configuration may obtain a similarly efficient refinement based on their specific experience, a systematic computation methodology as AVBP+MMG3D allows to retain this efficiency for a large variety of flows.

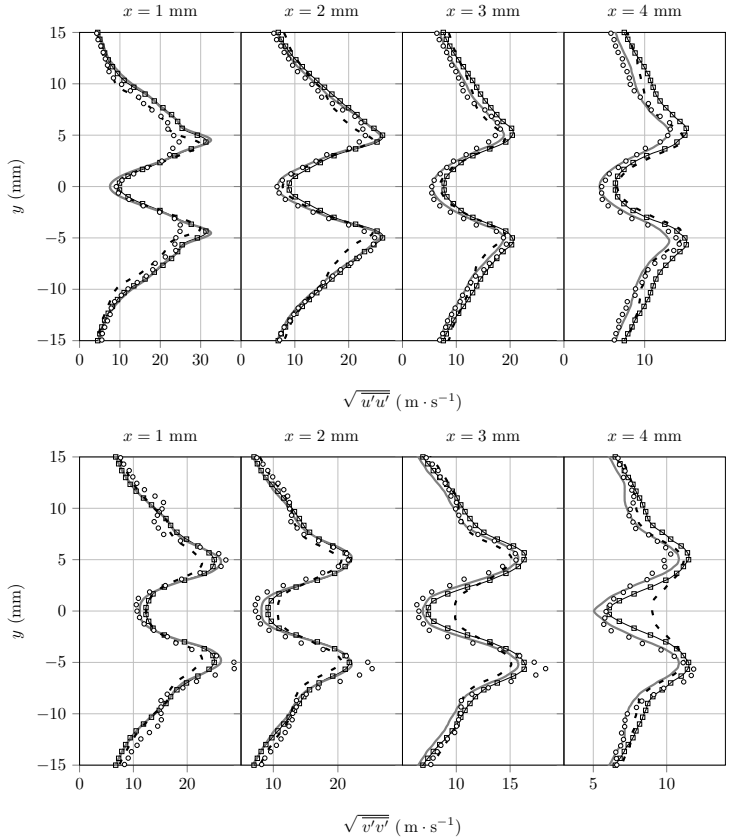

Fig. 16 $\dot{m} = 4.29\,\mathrm{g}\cdot\mathrm{s}^{-1}$ case: comparison of the radial distribution of turbulence intensities in axial (top) and tangential (bottom) direction at four axial locations (from left to right $x = 1, 2, 3, 4\,\mathrm{mm}$). Coarse mesh (- - -); mesh adapted AD 1 (—□—); mesh adapted AD 2 (——) and experiments PIV (○).

5 Conclusion

A mesh refinement algorithm has been proposed that improves the prediction of pressure losses in Large Eddy Simulations of turbulent flow in swirlers at reasonable computational cost. The method is based on an existing compressible LES code (AVBP) and mesh refinement program (MMG3D). Mesh refinement is done only a few times (1 to 3) during a complete simulation and it uses only mean flow information. It is performed outside the LES solver and needs no intrusive modification of the solver itself. The metric that defines the local mesh size is

the time-averaged value of the kinetic energy dissipation $\overline{\tilde{\Phi}}$. When this field is sufficiently well resolved, both pressure losses and velocity fields are correctly predicted.

The method is validated on two cases: (1) the flow through a diaphragm and (2) the flow through an industrial swirler used for helicopter engines. However, the method is not specific to these flows but may be applied to other flows. Results confirm its power in these two cases and suggest that it can be used for other LES solvers where it would bring a systematic, user-independent method to define meshes for LES tools.

Acknowledgements The research leading to these results has received funding from the European Research Council under the European Union's Seventh Framework Program (FP/2007-2013) / ERC Grant Agreement ERC-AdG 319067-INTECOCIS. This work was granted access to the HPC resources of CINES under the allocation 2016-[x20162b7036] made by GENCI. The authors acknowledge the support of C. Dobrzynski and A. Froehly from INRIA Bordeaux for the support on the MMG3D library.

Appendix: Comparison between hexahedral and tetrahedral meshes

This paper focused on automatic mesh adaptation for swirled flows using tetrahedral meshes. However, the methodology and the refinement sensor are not limited to any particular mesh element type. This appendix compares the LES results obtained with the same solver (AVBP) on the tetrahedral AD 2 mesh and on an unstructured fully hexahedral mesh H 2 (Fig. 17). The smallest element size of the hexahedral H 2 mesh is equivalent to that of the AD 2 mesh, and hence the explicit time-step is also equivalent, see Table 4. All other numerical parameters for the H 2 LES are chosen identical to the ones for AD 2 which are discussed in Sec. 2.

Table 4 Summary of the results between hexahedral H 2 and tetrahedral AD 2 meshes

	Tetrahedral AD 2	Hexahedral H 2
time step ($\times 10^{-7}$ s)	0.35	0.33
number of cells ($\times 10^6$)	10.8	6.8
number of CPU hours	20h20	20h48
ΔP error	-0.7%	7.8%
error on swirl number S at $x = 2\,\text{mm}$	4.3%	25.0%

As shown on Fig. 17, result on the total mean dissipation field $\overline{\tilde{\Phi}}$ on the hexahedral mesh is very close to one obtained on the AD 2 mesh although some differences are naturally visible. In particular, the boundary layers has been well captured despite some differences on the plug tip and on the mixing zone downstream the primary nozzle. Fig. 18 shows a comparison of the mean axial velocity fields downstream of the swirler exit. Results are similar close to the nozzle exit ($x < 3\,\text{mm}$) with some discrepancies downstream ($x > 4\,\text{mm}$).

More quantitatively, Fig. 19 and Fig. 20 show the first and second order moment statistics at four axial locations (from left to right $x = 1, 2, 3, 4\,\text{mm}$, see Fig. 13). For the mean axial and tangential velocity profiles (Fig. 19) at $x = 1\,\text{mm}$

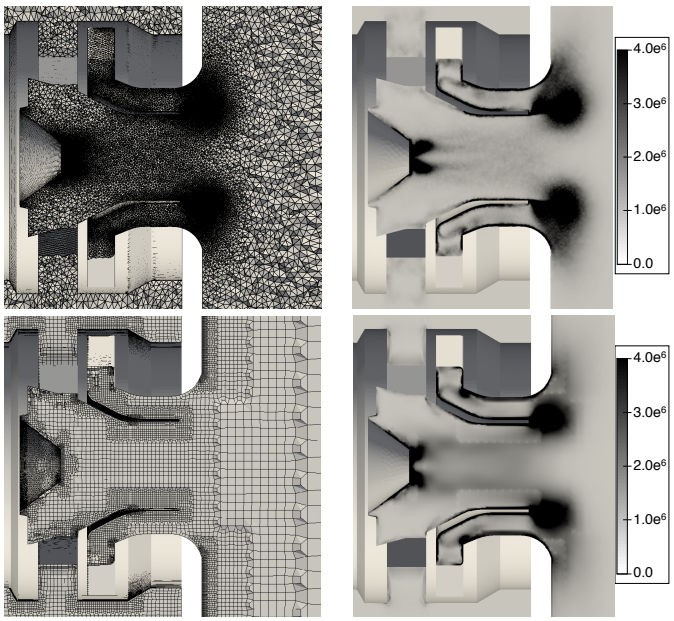

Fig. 17 $\dot{m} = 4.29\,\mathrm{g}\cdot\mathrm{s}^{-1}$ case: meshes (left) and fields of $\overline{\dot{\Phi}}$ in $\mathrm{W}\cdot\mathrm{m}^{-3}$ (right) for the tetrahedral AD 2 (up) and hexahedral (bottom) meshes.

and $x = 2\,\mathrm{mm}$, results are very similar between H 2 and AD 2 meshes. The discrepancies observed downstream at $x = 3\,\mathrm{mm}$ and $x = 4\,\mathrm{mm}$ for the hexahedral H 2 mesh are due to the local mesh coarsening imposed by the hexahedral mesher to avoid hanging nodes (see Fig. 17 left column bottom). The same observations can be made regarding the radial distribution of turbulence intensities in axial (top) and tangential (bottom) direction on Fig. 20.

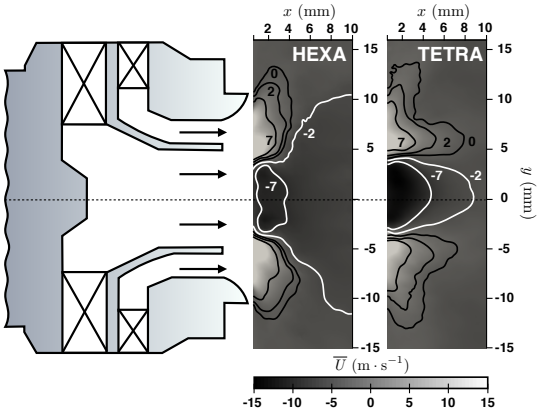

Fig. 18 Comparison of the mean axial velocity from LES on hexahedral mesh (center) and AD 2 tetrahedral mesh (right) for the $\dot{m} = 4.29\,\mathrm{g}\cdot\mathrm{s}^{-1}$ case. A schematic representation of the swirl injector is depicted on the left. White lines denotes negative mean velocity contours at -7 and $-2\,\mathrm{m}\cdot\mathrm{s}^{-1}$. Positive and zero mean velocity contours of 7, 2 and $0\,\mathrm{m}\cdot\mathrm{s}^{-1}$ are shown with black line.

The swirl number obtained at $x = 2\,\text{mm}$ is 0.57. This is a 25% error compared to the theoretical value and higher than the one obtained with the tetrahedral meshes. Comparison of the results between hexahedral and AD 2 tetrahedral meshes is given in table 4.

Finally, the QOI (the time averaged total mean dissipation field) in the right column of Fig. 17 clearly indicate the same regions that need to be refined to improve pressure loss predictions. Provided an automatic re-mesher is available, the same methodology can therefore be applied regardless of the mesh element type.

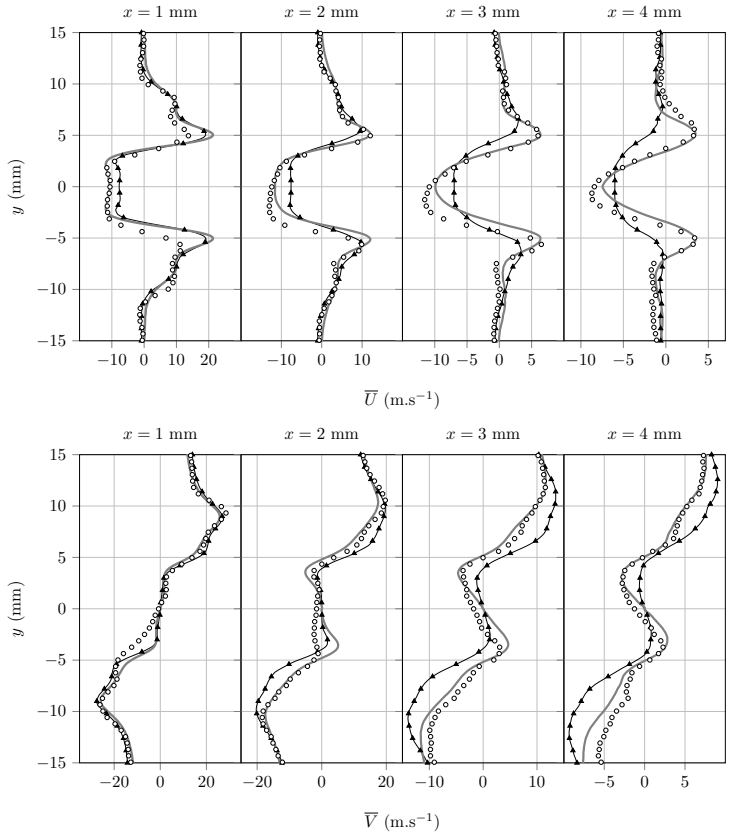

Fig. 19 $\dot{m} = 4.29\,\text{g}\cdot\text{s}^{-1}$ case: comparison of the radial distribution of mean axial (top) and tangential (bottom) velocity at four axial locations (from left to right $x = 1, 2, 3, 4\,\text{mm}$). Hexahedral H 2 mesh (—▲—); mesh adapted AD 2 (——) and experiments PIV (○).

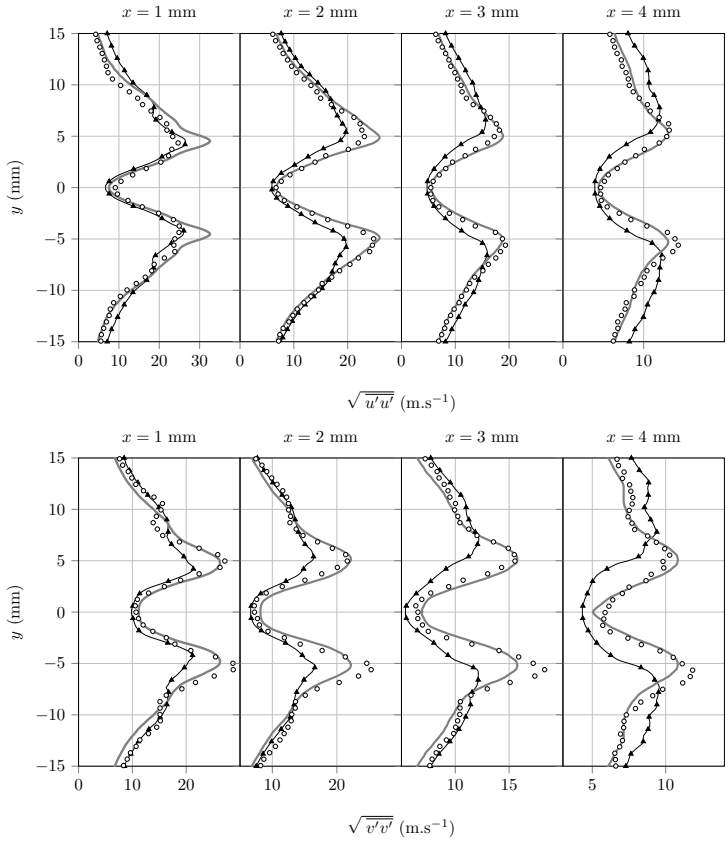

Fig. 20 $\dot{m} = 4.29\,\mathrm{g}\cdot\mathrm{s}^{-1}$ case: comparison of the radial distribution of turbulence intensities in axial (top) and tangential (bottom) direction at four axial locations (from left to right $x = 1, 2, 3, 4\,\mathrm{mm}$). Hexahedral H 2 mesh (—▲—); mesh adapted AD 2 (——) and experiments PIV (○).

References

1. Syred, N.: A review of oscillation mechanisms and the role of the precessing vortex core (PVC) in swirl combustion systems. Prog. Energ. Combust. **32**(2), 93–161 (2006)
2. Huang, Y., Sung, H.G., Hsieh, S.Y., Yang, V.: Large-eddy simulation of combustion dynamics of lean-premixed swirl-stabilized combustor. J. Prop. Power **19**(5), 782–794 (2003)
3. Moureau, V., Domingo, P., Vervisch, L.: From large-eddy simulation to direct numerical simulation of a lean premixed swirl flame: Filtered laminar flame-pdf modeling. Combust. Flame **158**(7), 1340–1357 (2011)
4. Roux, S., Lartigue, G., Poinsot, T., Meier, U., Bérat, C.: Studies of mean and unsteady flow in a swirled combustor using experiments, acoustic analysis and large eddy simulations. Combust. Flame **141**, 40–54 (2005)
5. Apte, S.V., Mahesh, K., Moin, P., Oefelein, J.C.: Large-eddy simulation of swirling particle-laden flows in a coaxial-jet combustor. Int. J. Multiphase Flow **29**(8), 1311–1331 (2003)
6. Falese, M., Gicquel, L.Y., Poinsot, T.: LES of bifurcation and hysteresis in confined annular swirling flows. Comput. Fluids **89**, 167–178 (2014)
7. Sankaran, V., Menon, S.: LES of spray combustion in swirling flows. J. Turb. **3**, 011 (2002)

8. Huang, Y., Yang, V.: Dynamics and stability of lean-premixed swirl-stabilized combustion. Prog. Energy Comb. Sci. **35**(4), 293–364 (2009)
9. Gicquel, L.Y.M., Staffelbach, G., Poinsot, T.: Large eddy simulations of gaseous flames in gas turbine combustion chambers. Prog. Energy Comb. Sci. **38**(6), 782–817 (2012)
10. Barré, D., Kraushaar, M., Staffelbach, G., Moureau, V., Gicquel, L.Y.M.: Compressible and low Mach number LES of a swirl experimental burner. CR - Mec. **341**, 277–287 (2013)
11. Falese, M.: A study of the effects of bifurcations in swirling flows using Large Eddy Simulation and mesh adaptation. Ph.D. thesis, Université de Toulouse (2013)
12. Choi, H., Moin, P.: Grid-point requirements for large eddy simulation: Chapman' s estimates revisited. Physics of Fluids **24**, 011,702–5 (2012)
13. Boudier, G., Gicquel, L.Y.M., Poinsot, T., Bissières, D., Bérat, C.: Effect of mesh resolution on Large Eddy Simulation of reacting flows in complex geometry combustors. Combust. Flame **155**(1-2), 196–214 (2008)
14. Hertel, C., Fröhlich, J.: Error reduction in LES via adaptive moving grids. In: Qual. Reliab. Large-Eddy Simulations II, vol. 16, pp. 309–318 (2011)
15. Frey, P.J., Alauzet, F.: Anisotropic mesh adaptation for CFD computations. Computer methods in applied mechanics and engineering **194**(48), 5068–5082 (2005)
16. Loseille, A., Dervieux, A., Alauzet, F.: Fully anisotropic goal-oriented mesh adaptation for 3d steady Euler equations. Journal of computational physics **229**(8), 2866–2897 (2010)
17. Rai, M.M., Anderson, D.: The use of adaptive grids in conjunction with shock-capturing methods. In: 11th AIAA Fluid Dynamics Conference, AIAA 81-1012 (1981)
18. Berger, M.J., Oliger, J.: Adaptive mesh refinement for hyperbolic partial differential equations. J. Comput. Phys. **53**(3), 484–512 (1984)
19. Dapogny, C., Dobrzynski, C., Frey, P.: Three-dimensional adaptive domain remeshing, implicit domain meshing, and applications to free and moving boundary problems. J. Comput. Phys. **262**, 358–378 (2014)
20. Mitran, S.M.: A comparison of adaptive mesh refinment approaches for large-eddy simulation. In: 3rd AFOSR International Conference on DNS/LES (2001)
21. Lohner, R., Baum, J.D.: Adaptive h-refinement on 3D unstructured grids for transient problems. Int. J. Numer. Meth. Fluids **14**(12), 1407–1419 (1992)
22. Majewski, J., Rokicki, J.: Anisotropic mesh adaptation in the presence of complex boundaries. In: ADIGMA - A Eur. Initiat. Dev. Adapt. Higher-Order Var. Methods Aerosp. Appl., pp. 441–453 (2010)
23. Majewski, J., Szatys, P., Rokicki, J.: Anisotropic Adaptation for Simulation of High-Reynolds Number Flows Past Complex 3D Geometries. In: N. Kroll, C. Hirsch, F. Bassi, C. Johnston, K. Hillewaert (eds.) IDIHOM Ind. High-Order Methods - A Top-Down Approach, Notes on Numerical Fluid Mechanics and Multidisciplinary Design, vol. 128, pp. 101–124 (2015)
24. Lombardini, M., Deiterding, R.: Three-dimensional parallel adaptive mesh refinement simulations of shock-driven turbulent mixing in plane and converging geometries. In: 21st International Conference on Parallel Computational Fluid Dynamics (2009)
25. Zhang, B., Wang, T., Gu, C.G., Dai, Z.Y.: An adaptive control strategy for proper mesh distribution in large eddy simulation. J. Hydrodyn. Ser. B **22**(6), 865–870 (2010)
26. Benard, P., Balarac, G., Moureau, V., Dobrzynski, C., Lartigue, G., D'Angelo, Y.: Int. J. Numer. Meth. Fluids **81**, 719–740
27. Bejan, A.: Entropy generation minimization: The new thermodynamics of finite-size devices and finite-time processes. J. Applied Phy. **79**(3), 1191–1218 (1996)
28. Kock, F., Herwig, H.: Entropy production calculation for turbulent shear flows and their implementation in CFD codes. Int. J. Heat Fluid Flow **26**(4), 672–680 (2005)
29. McEligot, D.M., Walsh, E.J., Laurien, E., Spalart, P.R.: Entropy generation in the viscous parts of turbulent boundary layers. J. of Fluids Eng. **130**(6), 1–12 (2008)
30. Prigogine, I.: Time, structure, and fluctuations. Science **201**(4358), 777–785 (1978)
31. Horne, W.C., Karamcheti, K.: Extrema principles of entropy production and energy dissipation in fluid mechanics. Tech. Rep. NASA-TM-100992 (1988)
32. Denton, J.D.: Loss Mechanisms in Turbomachines. J. Turbomach. **115**, 621–656 (1993)
33. Lax, P.: Hyperbolic systems of conservation laws II. Comm. Pure Appl. Math. **10**(4), 537–566 (1957)
34. Osher, S., Chakravarthy, S.: High Resolution Schemes and the Entropy Condition. SIAM J. Num. Anal. **21**(5), 955–984 (1984)
35. Zeman, O.: Dilatation dissipation: the concept and application in modeling compressible mixing layers. Phys. Fluids **2**, 178–188 (1990)

36. Sagaut, P.: Large Eddy Simulation for Incompressible Flows. Springer-Science (1998)
37. Piomelli, U.: Large-Eddy simulation: achievements and challenges. Prog. Aero. Sci. **35**(4), 335–362 (1999)
38. Biswas, R., Strawn, R.C.: Tetrahedral and hexahedral mesh adaptation for CFD problems. App. Num. Math. **26**, 135–151 (1998)
39. Schønfeld, T., Rudgyard, M.: Steady and unsteady flow simulations using the hybrid flow solver avbp. AIAA J. **37**(11), 1378–1385 (1999)
40. Selle, L., Lartigue, G., Poinsot, T., Koch, R., Schildmacher, K.U., Krebs, W., Prade, B., Kaufmann, P., Veynante, D.: Compressible large eddy simulation of turbulent combustion in complex geometry on unstructured meshes. Combust. Flame **137**(4), 489–505 (2004)
41. Colin, O., Rudgyard, M.: Development of high-order Taylor-Galerkin schemes for unsteady calculation. J. Comput. Phys. **162**(2), 338–371 (2000)
42. Poinsot, T., Lele, S.K.: Boundary conditions for direct simulations of compressible viscous flows. J. Comput. Phys. **101**(1), 104–129 (1992)
43. Thompson, K.W.: Time dependent boundary conditions for hyperbolic systems. J. Comput. Phys. **68**(1), 1–24 (1987)
44. Rudy, D., Strikwerda, J.: A non-reflecting outflow boundary condition for subsonic navier-stokes calculations. J. Comp. Phy. **36**, 55–70 (1980)
45. Nicoud, F., Baya Toda, H., Cabrit, O., Bose, S., Lee, J.: Using singular values to build a subgrid-scale model for large eddy simulations. Phys. Fluids **23** (2011)
46. Baya Toda, H., Cabrit, O., Balarac, G., Bose, S., Lee, J., Choi, H., Nicoud, F.: A subgrid-scale model based on singular values for LES in complex geometries. In: Proc. Summer Progr., pp. 193–202. Center for Turbulence Research (2010)
47. Baya Toda, H., Cabrit, O., Truffin, K., Gilles, B., Nicoud, F., Applications, E., Energy, T., Techniques, A.: A dynamic procedure for advanced subgrid-scale models and wall-bounded flows. In: Seventh Int. Symp. Turbul. Shear Flow Phenom. (2011)
48. Rieth, M., Proch, F., Stein, O.T., Pettit, M.W.A., Kempf, A.M.: Comparison of the Sigma and Smagorinsky LES models for grid generated turbulence and a channel flow. Comput. Fluids **99**, 172–181 (2014)
49. Idel'Cik, I.: Memento des pertes de charge. Eyrolles (1969)
50. White, F.: Fluid Mechanics. McGraw-Hill series in mechanical engineering (2011)
51. Hunt, J., Wray, A., Moin, P.: Eddies, stream, and convergence zones in turbulent flows. In: Proceedings of the summer program, pp. 193–208. Center for Turbulence Research (1988)
52. Merkle, K.: Einfluss gleich- und gegensinniger Drehrichtung der Verbrennungsluftströme auf die Stabilisierung turbulenter Doppeldrall-Diffusionsflammen. Ph.D. thesis, Universität Fridericiana Karlsruhe (2006)
53. Celik, I.B., Ghia, U., Roache, P.J., Freitas, C.J.: Procedure for Estimation and Reporting of Uncertainty Due to Discretization in CFD Applications. J. Fluids Eng. **130**(7) (2008)
54. Lilley, D.G.: Swirl Flows in Combustion: A Review. AIAA J. **15**(8), 1063–1078 (1977)
55. Midgley, K., Spencer, A., McGuirk, J.J.: Unsteady flow structures in radial swirler fed fuel injectors. J. Eng. Gas Turb. and Power **127**(4), 755–764 (2005)
56. Westerweel, J.: On velocity gradients in PIV interrogation. Exp. fluid **44**(5), 831–842 (2008)
57. Palies, P., Durox, D., Schuller, T., Candel, S.: The combined dynamics of swirler and turbulent premixed swirling flames. Combust. Flame **157**(9), 1698–1717 (2010)
58. Gupta, A.K., Lilly, D.G., Syred, N.: Swirl Flows. Abacus (1984)